Applied Catalysis B: Environmental 163 (2015) 352–360

Contents lists available at ScienceDirect

Applied Catalysis B: Environmental

journal homepage: www.elsevier.com/locate/apcatb

Photocatalytic degradation of phenol by semiconducting mixed oxides derived from Zn(Ga)Al layered double hydroxides

Julia Prince [a], Francisco Tzompantzi [b], G. Mendoza-Damián [b], F. Hernández-Beltrán [c], Jaime S. Valente [c,*]

[a] UAM-Azcapotzalco, Quimica de Materiales, Av. San Pablo # 180, 02200 Mexico, DF, Mexico
[b] UAM-Iztapalapa, Departamento de Quimica, Av. San Rafael Atlixco # 186, 09340 Mexico, DF, Mexico
[c] Instituto Mexicano del Petroleo, Eje Central # 152, 07730 Mexico, DF, Mexico

ARTICLE INFO

Article history:
Received 14 June 2014
Received in revised form 14 July 2014
Accepted 8 August 2014
Available online 17 August 2014

Keywords:
Layered double hydroxides
Semiconductors
Photocatalysis
Phenol degradation
Band gap energy

ABSTRACT

The synthesis and characterization of ZnAl and ZnGaAl layered double hydroxides and the mixed oxides derived from their calcination is presented. The semiconducting properties of the mixed oxides were analyzed by DR-UV–Vis. It was found that all mixed oxides are semiconductors with band gaps close to that of ZnO. Also, substitution of Al^{3+} for 5 or 10% wt. of Ga^{3+} decreases the band gap below that of ZnO, despite the fact that gallium oxide is a wide band gap semiconductor. Then, the photodegrading capabilities of the mixed oxides were tested using phenol, a very recalcitrant compound, as a probe. Nearly 80% of initial 40 ppm and 60% of initial 80 ppm of phenol were degraded in 6 h over ZnAl-3 and ZnGaAl-5% photocatalysts.

1. Introduction

Environmental remediation is a worldwide concern. Due to the expanding industrial activity, the amount of waste from chemical processes continues to increase, while the scientific community searches for feasible alternatives for their removal. Several contaminants are of particular interest. For instance, phenol and phenolic compounds are very commonly found in industrial wastewater effluvia [1]. Particularly, removal of phenol presents serious challenges, as this molecule is not biodegradable; it does not undergo direct photolysis by sunlight, and is not easily removed by conventional water treatment processes. Therefore, a number of chemical and catalytic alternatives are found in literature, including the use of semiconducting photocatalysts [2–18].

Semiconductors absorb a fraction of sunlight, mostly UV radiation, depending on their band gap energy. By absorption of a photon with energy equal to or greater than the band gap energy, an electron is excited from the valence band to the conduction band. The photogenerated electron–hole pairs react with electron donors and acceptors, creating highly reactive free radicals that in turn degrade the contaminant [19]. Therefore, increasing the absorption in the visible light range by reducing the band gap is a major goal, in order to increase effectiveness under sunlight radiation. Furthermore, the preparation of economic and reusable photocatalyst by simpler methods is continually searching for.

Photocatalysis using semiconducting mixed oxides derived from layered double hydroxides is a promising field, as these materials pose several advantages: they are economic, easy to prepare and reusable. Layered double hydroxides (LDHs), also known as hydrotalcite-like compounds, are a class of naturally occurring anionic clays. Their basic structure resembles that of brucite, $Mg(OH)_2$, in which a fraction x of divalent cations is isomorphously replaced by trivalent cations, rendering positively charged layers. The charge is electrically balanced by anionic species located in interlayer galleries, along with hydration water molecules. Given the variety of compounds with LDH structure that may be prepared, they are represented by the general formula: $[M_{(1-x)}{}^{2+} M_x{}^{3+} (OH)_2] A_{x/n}{}^{n-} \cdot mH_2O$. The divalent and trivalent cations are mainly those from the third and fourth periods of the periodic classification of the elements, *i.e.*, those with ionic radii similar to Mg^{2+} and that are capable of occupying the octahedral interstices of the brucite-like lattice. It is also possible to introduce three or even four metal cations in the layers, and to prepare LDHs with M^+-M^{3+} or M^{2+}-M^{4+} combinations [10,16]. Meanwhile, the charge-balancing anions A^{n-} are typically carbonates or halogens, although nearly any organic or inorganic anion may be intercalated [20,21]. Thus, the

* Corresponding author. Tel.: +52 55 91 75 84 44.
E-mail addresses: jsanchez@imp.mx, sanchezvalente@yahoo.com (J.S. Valente).

http://dx.doi.org/10.1016/j.apcatb.2014.08.019
0926-3373/

versatility and applicability of this family of compounds is quite vast [22,23].

Upon calcination, the structure progressively loses physisorbed and interlayer water molecules, layer OH groups, and charge-balancing anions. The layered structure collapses and a mixed oxide solid solution is formed. This mixed oxide typically presents large specific surface areas, thermal stability and synergic interactions between the different metal components. Therefore, LDH calcination products have found numerous applications in various catalytic processes [24–26].

Mixed oxides with semiconducting properties may be obtained by calcination of appropriate transition metal-containing LDHs. A wide variety of metal cations, such as Zn^{2+} and Ti^{4+}, may be introduced in the layers [10,11,13–17]. Their relative proportions may be varied in a fairly wide range. This affords the possibility of preparing semiconducting oxides with tunable properties. For instance, a series of Mg–Zn–Al mixed oxides have been shown to have dual adsorption–photodegrading capabilities in the elimination of 2,4-dichlorophenoxiacetic acid [11]. These solids were also effective for the degradation of phenol. Furthermore, it was demonstrated that impregnating MgAl LDHs with CeO_2 results in semiconducting solids which were efficient for the degradation of phenol, 4-chlorophenol and 2,4,6-trichlorophenol [12]. Photocatalytic applications of various LDHs (and/or mixed oxides resulting from their calcination) such as ZnAl [13–15,23], ZnTi [10,16] and ZnAlFe [17] have been reported.

Preparation of LDH materials is a rather simple way to obtain solid solutions by calcination at temperatures around 673–873 K, compared to thermal methods that require higher calcination temperatures, thus affording the possibility of band gap engineering. GaN–ZnO solid solutions have been widely studied as photocatalysts for water splitting [27]; the solid solution has a lower band gap than pure GaN or ZnO [28]. Indium–gallium–zinc oxide thin films have also been investigated as transistors for electronic devices [29]. Gallium-doped ZnO nanofibers revealed greater carrier concentration and electron mobility than the undoped ZnO sample [30]. Furthermore, it was recently reported that substituting aluminum for gallium increases the electron donor density in LDH thin films [31].

However, rather few reports are found concerning mixed $ZnO–Ga_2O_3$ solid solutions and their applications as photocatalysts. For instance, the $GaZn/TiO_2$ system was reported to be more efficient than the Zn/TiO_2 system for phenol removal [18]. The amount of Ga (up to 15%) was observed to improve the photocatalytic activity.

Thus, the present work reports a study on the photocatalytic performance of Zn(Al)O mixed oxides, derived from ZnAl LDHs with varying molar ratios (Zn/Al = 2, 3), as well as the influence of the isomorphic substitution of a fraction of Al^{3+} by Ga^{3+} in the LDHs structure. The substitution was carried out on a LDH with $Zn^{2+}/(Ga^{3+} + Al^{3+})$ molar ratio of 3, using 5 and 10 wt.% Ga. The crystalline structure, textural and morphological properties and band gap edges were studied, and the catalysts were tested for the photocatalytic degradation of phenol at relatively high concentrations, similar to those that may be found on some industrial effluents [1,32].

2. Experimental

2.1. Synthesis of LDHs

ZnAl LDHs with Zn/Al molar ratios of 2 and 3 and ZnGaAl LDHs with M^{2+}/M^{3+} molar ratio of 3 and 5 or 10 wt.% of gallium were prepared by the coprecipitation at low supersaturation method. Two separate solutions were prepared, an alkaline solution of KOH and K_2CO_3 (2 M), and a metallic solution (1 M) containing $ZnCl_2$, $AlCl_3·6H_2O$ and $Ga(NO_3)_3·xH_2O$ (where indicated) in the required proportions. Both solutions were added simultaneously at a controlled rate to a glass reactor with mechanical stirring, keeping the pH constant at 8. The resulting precipitate was aged for 18 h at 353 K, then washed abundantly with bidistilled water, and dried at 373 K overnight. The powdered solid was then contacted with a 2 M solution of K_2CO_3, and stirred at 353 K for 4 h, in order to exchange chloride anions for carbonate. The solid was then filtered, washed exhaustively with bidistilled water, and dried at 373 K. This anion-exchange procedure was carried out twice to ensure the complete exchange of chloride ions. Solids were named according to their chemical composition. Zn–Al LDHs were named *x*ZnAl, where *x* stands for the Zn^{2+}/Al^{3+} molar ratio. Zn–Ga–Al LDHs all have an M^{2+}/M^{3+} molar ratio of 3, and were named ZnGaAl-*y*, where *y* is the nominal weight percent of gallium. Parts of the prepared solids were calcined at 773 K for 6 h for characterization and photocatalytic testing. Calcined solids were named *x*ZnAl-c and ZnGaAl-*y*c.

2.2. Photocatalytic tests

Two different stock solutions were prepared, containing 0.42 mmol L^{-1} (40 ppm) and 0.85 mmol L^{-1} (80 ppm) of phenol. Then, for each test, a 200 mL aliquot was taken, and 200 mg of the activated (calcined) catalyst were added. The reaction mixture was mechanically stirred in the dark for 1 h to allow contact of the test molecule to the catalyst. Afterwards, solutions were irradiated with UV light using a Pen Ray Power Supply lamp, 115 V, λ = 254 nm, intensity = 4400 $\mu W\,cm^{-2}$, light length 1(1/8) in., without filter, which was immersed in the solution.

The remaining amount of phenol at a given time was determined by UV–Vis spectroscopy, using a Cary 100 spectrophotometer with integration sphere. Phenol concentration is directly proportional to absorbance, by the Beer–Lambert law: $A = \varepsilon bC$; where A is the absorbance at 269 nm, ε is the molar absorptivity coefficient, b is the path length (0.01 m), and C is the molar concentration. A calibration curve was constructed from 0.16 to 0.90 mmol L^{-1}, obtaining a correlation coefficient $r^2 = 0.978$, and a slope $\varepsilon b = 1364$.

2.3. Characterization techniques

2.3.1. Chemical analysis

The chemical composition of solids was determined in a Perkin–Elmer model Optima 3200 Dual Vision by inductively coupled plasma atomic emission spectrometry (ICP-AES).

2.3.2. X-ray diffraction

The X-ray diffraction patterns of the samples were measured in a θ–θ Bruker D-8 Advance diffractometer with Cu Kα radiation, a graphite secondary-beam monochromator, and a scintillation detector. Diffraction intensity was measured between 4 and 80°, with a 2θ step of 0.02° and a counting time of 9 s per point.

2.3.3. Transmission electron microscopy

Powdered samples were analyzed through transmission electron microscopy (TEM) in a Jeol 200Kv JEM-2200FS. The microscope is equipped with a Schottky-type field emission gun in ultra-high-resolution (UHR) configuration (C_s = 0.5 mm; C_c = 1.1 mm; point-to-point resolution, 0.19 nm) and in-column omega-type energy filter. Samples were dispersed in ethanol before placing them on the copper grid with Formvar support.

2.3.4. Scanning electron microscopy

SEM analysis was carried out in a Philips XL30 ESEM with an acceleration voltage of 25 kV. The chemical composition was

Table 1
Chemical compositions of LDHs and unit cell parameters of both as-synthesized and calcined solids.

Sample	General formula	M^{2+}/M^{3+} ratio	Unit cell parameters (Å)			
			c^a	a^a	c^b	a^b
2ZnAl	$[Zn_{0.66}\ Al_{0.34}\ (OH)_2]\ (CO_3)_{0.17}{}^{2-}\cdot H_2O$	1.93	22.804	3.076	5.205	3.221
3ZnAl	$[Zn_{0.72}\ Al_{0.28}\ (OH)_2]\ (CO_3)_{0.14}{}^{2-}\cdot H_2O$	2.57	22.804	3.074	5.205	3.227
ZnGaAl-5	$[Zn_{0.74}\ Ga_{0.12}\ Al_{0.14}\ (OH)_2]\ (CO_3)_{0.13}{}^{2-}\cdot H_2O$	2.87	22.901	3.092	5.205	3.239
ZnGaAl-10	$[Zn_{0.75}\ Ga_{0.21}\ Al_{0.04}\ (OH)_2]\ (CO_3)_{0.13}{}^{2-}\cdot H_2O$	3.06	22.902	3.101	5.198	3.248

[a] As-synthesized samples.
[b] Samples calcined at 773 K for 6 h.

examined using an energy-dispersive X-ray spectrometer (EDS) device attached to the microscope.

2.3.5. Textural analysis

The texture of the calcined samples was analyzed by N_2 adsorption–desorption at 77 K on a Quantachrome Autosorb-3B apparatus. Prior to the analysis, the samples were outgassed in a vacuum (10^{-5} Torr) at 623 K for 12 h. The surface areas were calculated by the Brunauer–Emmett–Teller (BET) method, and the pore size distribution and total pore volume were determined by the Brunauer–Joyner–Hallenda (BJH) method applied to the desorption branch.

2.3.6. UV–Vis spectroscopy

UV–Vis spectra were acquired using a Cary-100 (Varian) spectrophotometer. The band gap of a material can be estimated from the adsorption edge wavelength of the interband transition. The most accepted method for determining the band gap energy values of an insulator or semiconductor is by plotting the square root of the Kubelka-Munk function multiplied by the photon energy *versus* the photon energy and extrapolating the linear part of the rising curve to zero. For each material the energy of the forbidden band (E_g) was calculated in accord with the following equation:

$$E_g(\text{eV}) = 1239\left(\frac{b}{-a}\right) \quad (1)$$

where a and b are coefficients that were linearized in the appropriate region of the spectrum.

2.3.7. Total organic carbon

The evolution of the total organic carbon (TOC) during the photocatalytic degradation was followed using a TOC-VCEN Shimadzu analyzer (catalytic oxidation on Pt at 680 °C). Calibration runs were performed using a potassium phthalate calibration curve.

3. Results and discussion

3.1. Catalyst characterization

The chemical composition of the as-synthesized solids was determined by ICP-AES. The general formulas and the divalent to trivalent cation molar ratios are reported in Table 1. The lowering of the M^{2+}/M^{3+} molar ratio is due to an incomplete incorporation of metal cations. This phenomenon has been observed and reported previously [33]; it is mainly due to the different precipitation pH of each cation. A precipitation pH is determined based on the phase diagram of each metal. The pH was set at 8 in order to obtain an LDH phase. The incomplete incorporation of zinc can be explained by the smaller pH region of zinc precipitation, compared to that of aluminum [34]. Gallium and zinc have very similar precipitation intervals. This allows a better incorporation of zinc to the LDH structure when the gallium amount increases (see the M^{2+}/M^{3+} molar ratios reported in Table 1).

The X-ray diffraction patterns of as-synthesized ZnAl and ZnGaAl layered double hydroxides (LDHs) with variable chemical compositions are displayed in Fig. 1. The diffraction peaks correspond to a crystalline LDH phase with a 3R polytype (PDF 00-014-0191). The first two sharp diffraction peaks correspond to (0 0 3) and (0 0 6) planes from which the interlayer distance, *i.e.*, the *c* unit cell parameter, was calculated (Table 1). The interlayer distance agrees well with the intercalation of carbonate as interlayer anion, as expected due to the anion-exchange procedures. In-plane diffraction peaks appear at higher angles; around 60° 2θ is the (1 1 0) plane, which indicates the average cation to cation distance (*a* unit cell parameter, Table 1). The inclusion of Ga^{3+} to the LDH lattice is verified by the proportional increase in *a* parameter, in agreement with Vegard's law, given that Ga^{3+} has a larger ionic radius than Al^{3+} (0.62 *vs.* 0.53 Å, [35]). On the other hand, *a* parameters of samples 2ZnAl and 3ZnAl do not follow the expected trend. The ionic radius of Al^{3+}, 0.53 Å, is smaller than that of Zn^{2+} (0.74 Å) [35], thus sample 3ZnAl, with greater amounts of zinc than 2ZnAl, should present a larger *a* unit cell parameter. The calculated *a* parameters indicate an incomplete incorporation of zinc to the brucite-like sheets of the LDH and the formation of ZnO nanocrystals, as will be discussed below.

After calcination, XRD patterns in Fig. 2 reveal that all ZnAl and ZnGaAl LDHs are completely transformed into mixed metal oxides, in which the only diffraction peaks correspond to hexagonal ZnO (PDF 00-036-1451), indicating that trivalent cations are evenly distributed in the oxide network. Indeed, the attainment of Zn(Al, Ga)O solid solutions is verified by the slightly shifted *a* unit cell parameters, taking as a reference *a* = 3.25 Å for ZnO. The variation of this parameter agrees well with the trend expected from Vegard's law for solid solutions (Table 1), considering the ionic radii of Zn^{2+}, Al^{3+} and Ga^{3+}. Addition of larger amounts of Al^{3+}, a small ion, decreases the *a* parameter. Contrarily, gallium brings about a slight increase in *a* parameters, which is proportional to the amount of Ga^{3+} (Table 1).

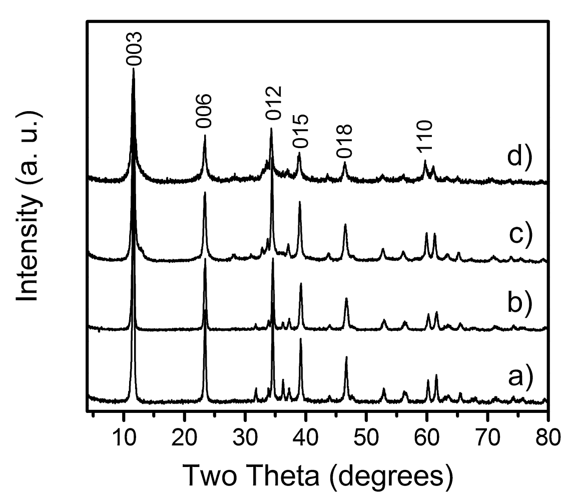

Fig. 1. X-ray diffraction patterns of as-synthesized solids: (a) 2ZnAl, (b) 3ZnAl, (c) ZnGaAl-5 and (d) ZnGaAl-10.

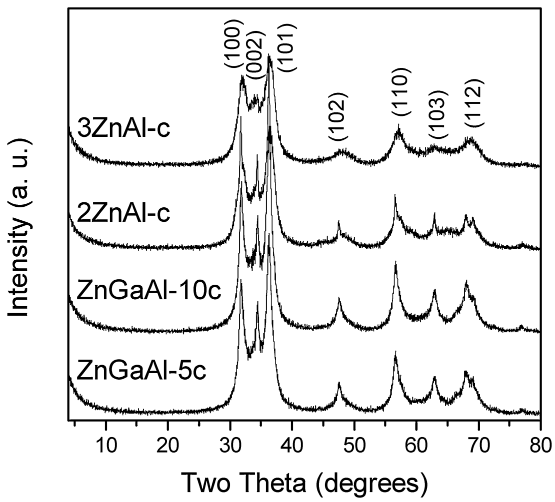

Fig. 2. X-ray diffraction patterns of mixed oxides obtained by calcination of LDHs.

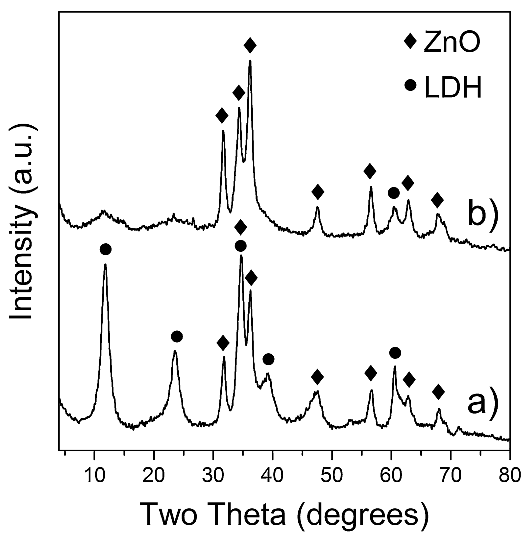

Fig. 3. X-ray diffraction patterns of samples (a) 3ZnAl-c and (b) ZnGaAl-5c recovered after photocatalytic reaction.

It is well known that calcined LDHs are capable of recovering their original layered structure due to their unique memory effect [20]. In order to determine whether this phenomenon occurs during photocatalytic degradation, the XRD patterns of samples 3ZnAl-c and ZnGaAl-5c after reaction were also measured (Fig. 3). A mixture of ZnO and LDH phases is appreciated on sample 3ZnAl-c after reaction, indicating that a partial reconstruction of the layered structure took place during the course of the reaction. Indeed, the position of the *1 1 0* peak appears shifted to a higher angle compared to that of as-synthesized 3ZnAl. The calculated *a* unit cell parameter of the sample after reaction is 3.055 Å, a value significantly smaller to the 3.074 Å of the pristine 3ZnAl LDH (Table 1). This indicates that the Zn/Al ratio of the reconstructed LDH phase is lower than that of 3ZnAl.

On the other hand, gallium-containing ZnGaAl-5c mostly retains the ZnO structure, as the extent and rate of the layered structure recovery depends closely on the chemical composition of the parent LDH. Only the *1 1 0* peak of the LDH phase is clearly discernible in the pattern of ZnGaAl-5c, indicating a preferential growth in this direction.

Band gap energies (E_g) of the mixed oxides, determined by diffuse reflectance UV–Vis (Table 2 and Fig. S1), range from 3.15 to 3.70 eV. The band gaps of ZnGaAl mixed oxides are comparable to the band gap of anatase TiO_2, a benchmark photocatalyst, which is of 3.0–3.2 eV [36]. Band gaps of the mixed oxides are also close to that of ZnO, 3.37 eV [37]. Only in the case of 2ZnAl-c, the measured band gap (3.70 eV) is greater than that of ZnO, probably due to the addition of larger quantities of Al^{3+}. However, the band gap of sample 3ZnAl-c is slightly smaller than that of ZnO. This indicates that the formation of a solid solution, attained by calcination of pure-phase LDHs, improves the semiconducting properties. For gallium-containing mixed oxides, the trends in band gap are also quite interesting when taking into account the band gap energies of the pure oxides: 8.8 eV for Al_2O_3 and 4.9–5.0 eV Ga_2O_3 [38]. Probably, Al^{3+} and Ga^{3+} cations introduce new energy levels, which bring about a slight decrease in band gap energy. Nonetheless, the fact that a smaller amount of gallium (5 wt.%) produces the solid solution with the lowest band gap (3.15 eV for ZnGaAl-5c *vs.* 3.18 eV in ZnGaAl-10c) is remarkable. In contrast, Robbins et al. [39] reported Ga-doped ZnO thin films prepared by plasma-enhanced chemical vapor deposition, where addition of Ga systematically increased the band gap from 3.3 eV for pure ZnO to 3.7 eV for films with a gallium fraction of 0.4.

It must be taken into account that calcination products of LDHs are actually mixed oxide solid solutions, and not a $ZnO/Al_2O_3/Ga_2O_3$ oxide mixture. Thus, the formation of a solid solution creates a new band structure where orbitals from Zn, Al, Ga and O combine to give a solid with lower band gap than that of ZnO.

Fig. 4 presents TEM images of samples ZnGaAl-5 and ZnGaAl-10 at different magnifications. As may be observed, particle sizes are of a few micrometers and both solids are composed of platelet-like particles, the typical morphology of coprecipitated LDHs. A closer look (Fig. 4b and d) shows that the platelets are composed of regularly stacked layers.

The crystalline structure of sample 3ZnAl was observed in detail by electron diffraction on TEM images, presented in Fig. 5. The main crystalline phase is the LDH; the image presents a large region of uniformly stacked layers with an interlayer distance that coincides well with that observed by XRD. Nevertheless, a small, well-defined ZnO nanocrystal of less than 10 nm in size is also observed. Most likely, there are very few of these ZnO nanoparticles throughout the solid, so they remain undetectable by XRD. Similar observations have been made previously; for instance, nanocrystalline γ-Al_2O_3 has been spotted by electron diffraction on calcined MgAl LDHs synthesized by sol–gel method, which was undetectable by XRD [40].

Table 2
Band gap energy and textural properties of calcined solids.

Sample	Band gap energy (eV)	BET surface area ($m^2\,g^{-1}$)	Pore volume ($cm^3\,g^{-1}$)	Average pore diameter (nm)	
				meso	macro
2ZnAl-c	3.70	112	0.241	3.4	71.1
3ZnAl-c	3.30	96	0.224	2.5	77.8
ZnGaAl-5c	3.15	70	0.263	2.6	110.7
ZnGaAl-10c	3.18	101	0.704	2.4	95.7

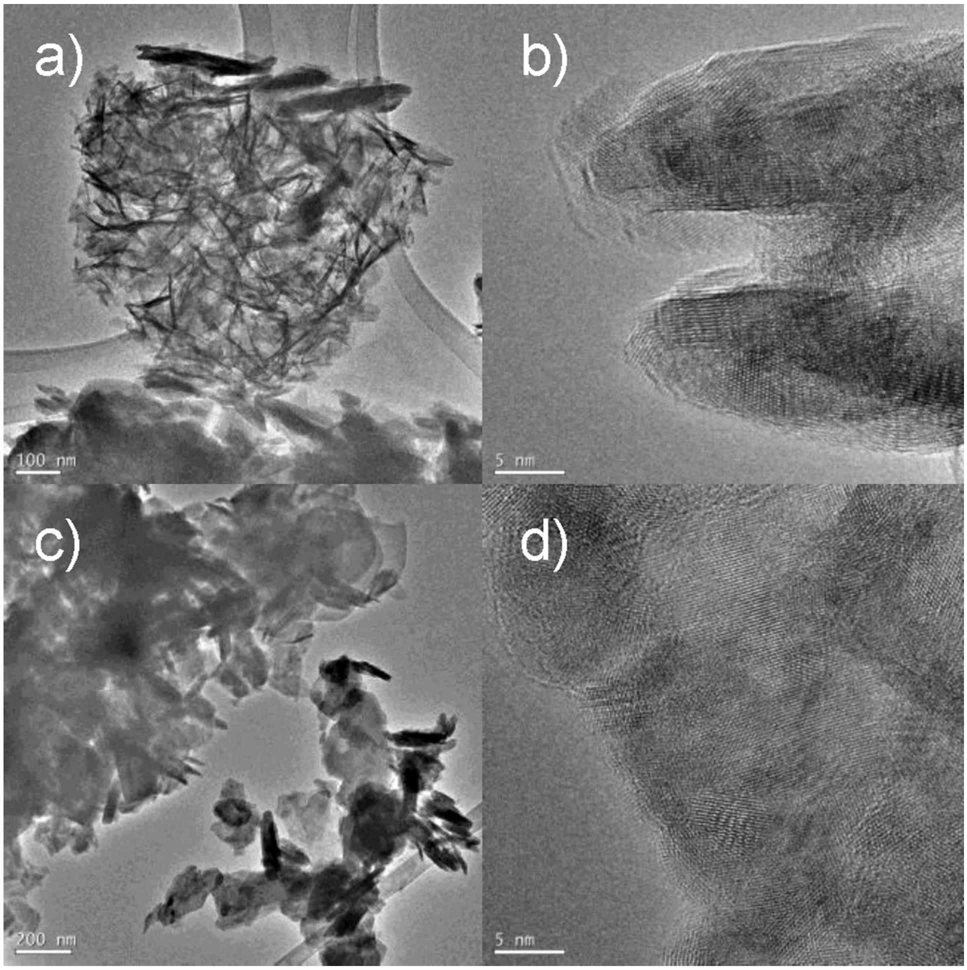

Fig. 4. TEM images of samples: (a and b) ZnGaAl-10 and (c and d) ZnGaAl-5.

After calcination (Fig. 5b), sample 3ZnAl-c displays only a well-defined ZnO phase. Furthermore, Fig. 6 displays TEM images of sample 3ZnAl-c before and after photocatalytic degradation, showing that there is no significant change in morphology in the used solids. However, some differences may be observed; for instance, after reaction, two different morphologies are clearly appreciated as distinct platelet-like particles arise from an irregular agglomeration of particles. The platelets are slightly larger after reaction due to the partial reconstruction of the LDH phase, in agreement with XRD observations. High resolution images from sample 3ZnAl-c recovered after photocatalytic degradation display two different crystalline arrangements (Fig. 7). Electron diffraction analyses reveal that they correspond to Zn(Al)O solid solution and ZnAl LDH, agreeing well with XRD results presented previously. The images depict clearly the superimposition of both crystalline phases. As mentioned previously, the reconstruction process's extent and velocity is closely related to the chemical composition and molar ratio of the precursor LDH, so that the exact phase distribution during the course of reaction is hard to determine. Furthermore, during calcination, interlayer carbonate is lost, and in this case the reconstructed LDH most likely incorporates OH^- as charge-balancing anion. The hydroxyl anion has been known to play a significant role in catalytic processes [41,42].

SEM images of sample ZnGaAl-5c before and after photocatalytic degradation (Fig. 8) present similar morphologies and particle sizes in both cases. Furthermore, EDS chemical mapping (Fig. 9) of Zn, Ga and Al in both as-synthesized and used solids display a uniform dispersion of all chemical components. No sintering or agglomeration of any metal was detected after use in the photocatalytic reaction. This indicates that the ZnO nanoparticles detected by HRTEM are highly dispersed throughout the main LDH particles. The surface chemical compositions of sample ZnGaAl-5c before and after catalytic tests are similar, and agree well with ICP-AES measurements, indicating that there is no metal leaching. Therefore, the photocatalytic degradation occurs through a purely heterogeneous process. The information provided by electron microscopy images indicates that the solids can be reusable.

Regarding the textural analyses by N_2 adsorption–desorption isotherms, calcined solids present Type II isotherms (Fig. S2), which correspond to monolayer-multilayer adsorption on macroporous solids [43]. This type of isotherm is characterized by a smooth, non-stepwise adsorption, associated with energetic heterogeneity in the adsorbent–adsorbate interactions. Furthermore, a thin hysteresis loop of the H3 type appears at high relative pressures. Due to the appearance of a hysteresis loop, this kind of isotherm may be termed Type IIb [43]. The loop indicates the presence of slit-shaped mesopores. This behavior is typical of LDH materials, where calcination brings about the disorderly collapse of plate-like particles, and the formation of a so-called house-of-cards structure [44]. Therefore, interparticle spacings are mainly responsible for the macroporosity of these solids.

Accordingly, pore size distribution plots (inset in Fig. S2) confirm that the majority of the pore volume corresponds to macropores, with a bimodal pore size distribution in which macropores range

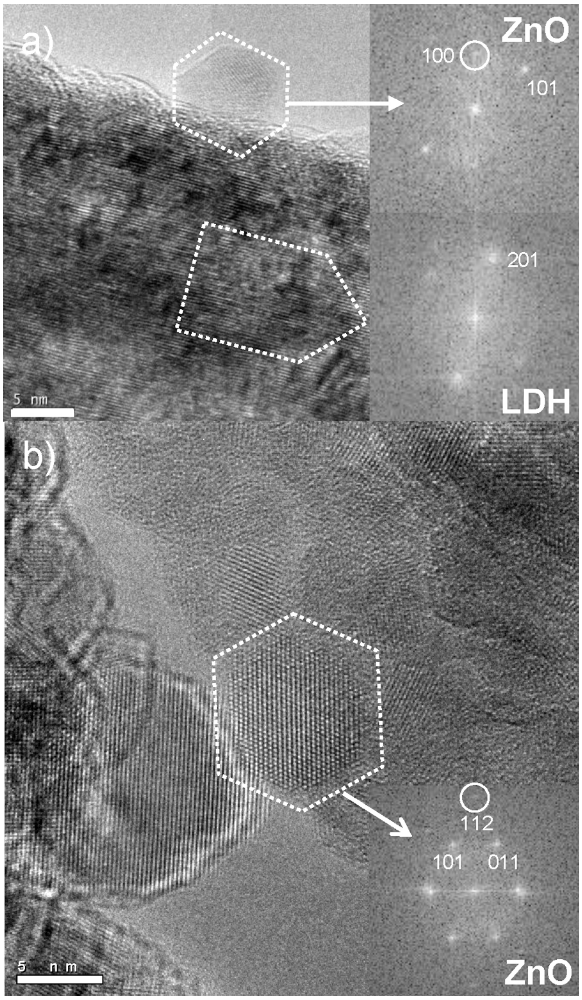

Fig. 5. HRTEM and electron diffraction of sample 3ZnAl: (a) as-synthesized and (b) calcined.

from 71 to 111 nm. Additionally, mesopores present an average diameter of 2–4 nm (Table 2). These pores may be formed by a craterization process that takes place in LDH materials during calcination [45], and by the irregular stacking of plate-like particles. BET surface areas, summarized in Table 2, range from 70 $m^2 g^{-1}$ for sample ZnGaAl-5c to 112 $m^2 g^{-1}$ for 2ZnAl-c.

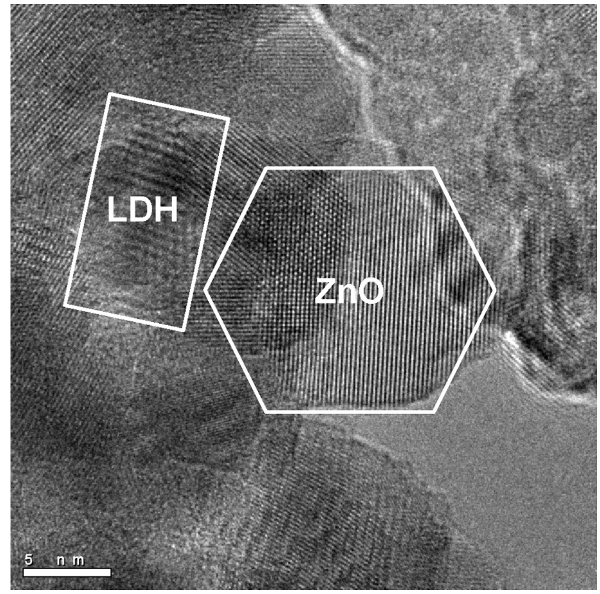

Fig. 7. HRTEM and electron diffraction of sample 3ZnAl-c, recovered after photocatalytic degradation.

3.2. Photocatalytic degradation

Calcined solids were tested for the photocatalytic degradation of phenol at relatively high concentrations, namely, 0.425 mmol L^{-1} and 0.85 mmol L^{-1} (40 and 80 ppm). These concentrations are close to those found in wastewaters from the petrochemical industry [1]. For the degradation of 40 ppm of phenol, solid 3ZnAl-c proved to be most effective, degrading *ca.* 80% of the contaminant in 6 h (Fig. 10). The photocatalytic activity of samples ZnGaAl-5c, ZnGaAl-10c and 2ZnAl-c is slightly less than 3ZnAl-c, and these samples degrade ~75% of the existing phenol. The complete phenol mineralization was confirmed by total organic carbon (TOC) analyses. Fig. S3 presents a comparison of the degradation profiles obtained by UV–Vis and by TOC on photocatalyst ZnGaAl-5c, showing a good agreement between both techniques.

It is interesting to notice how even though gallium decreases the band gap energy of the ZnGaAl-5c and ZnGaAl-10c solids, their photocatalytic activity is actually slightly lower than that of 3ZnAl-c. A possible explanation for this is that gallium might

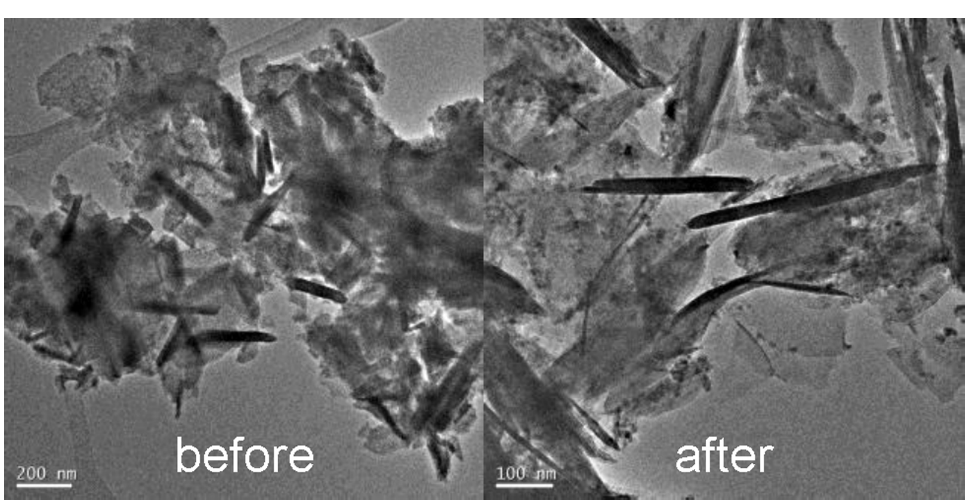

Fig. 6. TEM images of sample 3ZnAl-c before and after photocatalytic reaction.

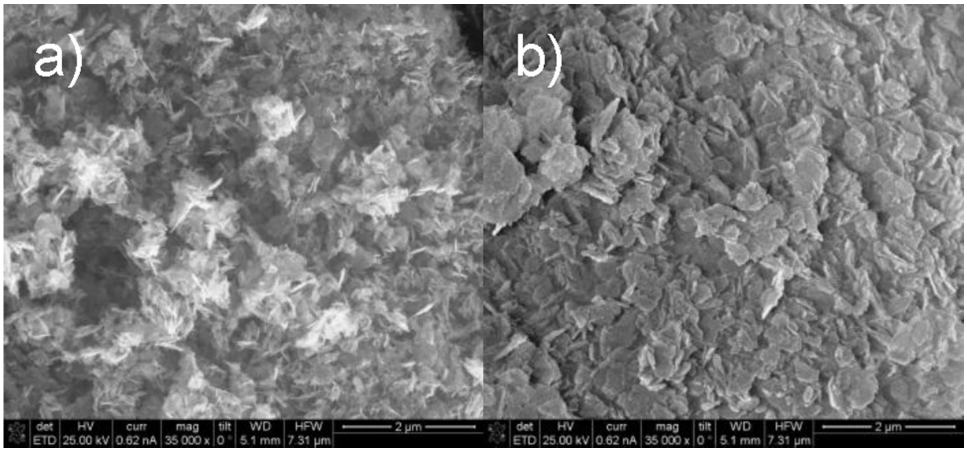

Fig. 8. SEM images of sample (a) ZnGaAl-5c and (b) ZnGaAl-5c after photocatalytic degradation.

increase the rate of electron–hole recombination because of its higher electronegativity than aluminum. This hypothesis is sustained by the fact that ZnGaAl-5c is slightly more active than its counterpart with 10 wt.% gallium, particularly during the first few hours (Fig. 10). Also in this sense, it must be remarked that textural properties, in particular the BET surface area, appear not to have a direct influence on the photocatalytic performance of solids. Samples with greatest surface area (2ZnAl-c and ZnGaAl-10c, Table 2) display the poorest degradation ability.

Another contributing factor for the observed differences in photocatalytic activity might be the different extent of layered structure recovery due to the memory effect. Gallium-containing samples preserve the mixed oxide structure with very little formation of LDH, while 3ZnAl-c presents both LDH and Zn(Al)O phases by the time the photodegradation is completed (Fig. 3). The reconstructed LDH incorporates OH^- as counter anion; photocatalytic properties of this meixnerite-like phase may be different to those of the pristine LDH. The fact that catalyst 3ZnAl-c retains a stable activity in time might indicate that both the mixed oxide and the reconstructed LDH phase are photocatalytically active. However, it is an open issue to determine the exact role of each crystalline phase.

Similarly, it has been reported that ZnAl and ZnCuAl are more photocatalitically active than ZnGa ZnCuGa LDHs for the conversion of carbon dioxide into methanol, despite ZnCuGa LDH presenting the lowest band gap energy, 3.5 eV, *vs.* 4.1 eV for ZnCuAl. The poorer performance of gallium-containing LDHs was attributed to differences in basicity and CO_2 affinities [46].

It is noteworthy that all solids present far greater photodegration than benchmark Degussa P25-TiO_2. In previous work, the degradation of 40 ppm of phenol was also attempted using MgZnAl LDHs with 5, 10 and 15% wt. of zinc [11]. The best result, obtained with MgZnAl-5, was *ca.* 70% degradation. All the solids presented here displayed better performance.

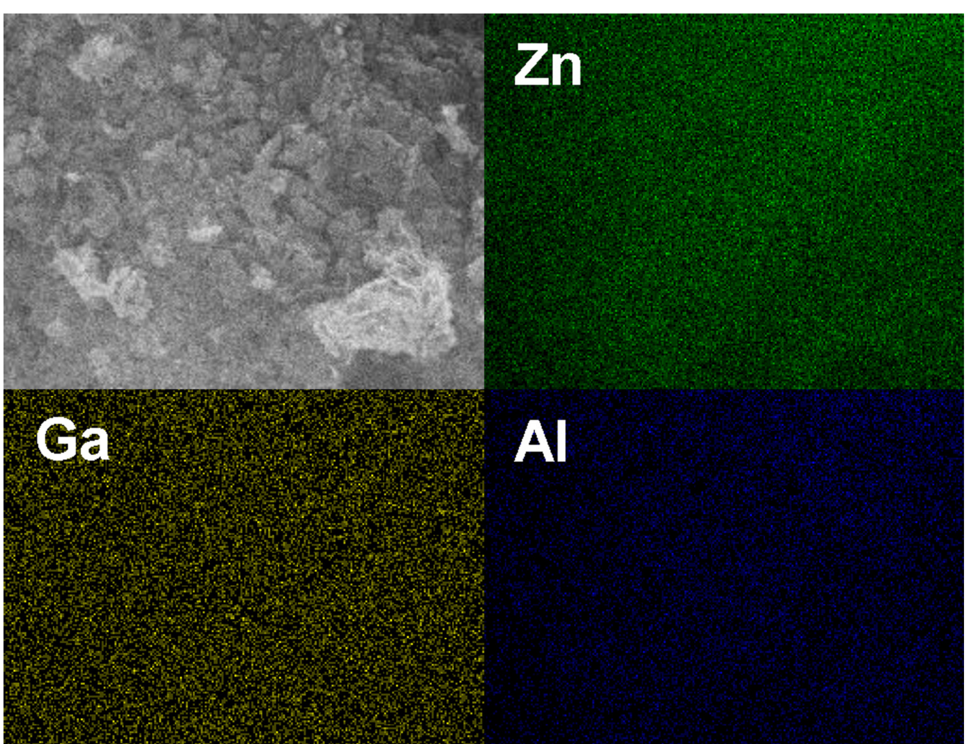

Fig. 9. SEM image and corresponding EDS chemical mapping of sample ZnGaAl-5c after photocatalytic reaction.

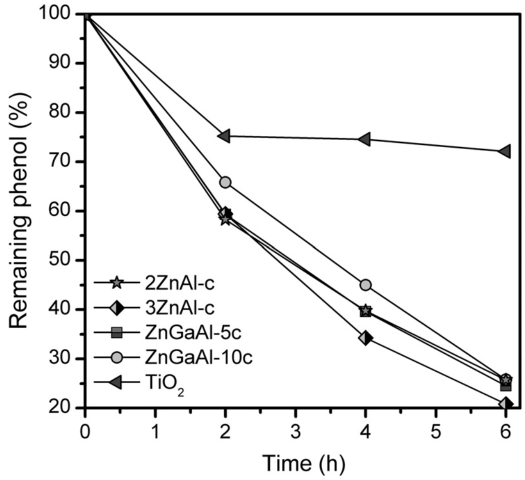

Fig. 10. Photocatalytic degradation of 40 ppm of phenol (0.425 mmol L^{-1}) by Zn(Al)O and Zn(Ga,Al)O mixed oxides, compared to Degussa P25 TiO_2.

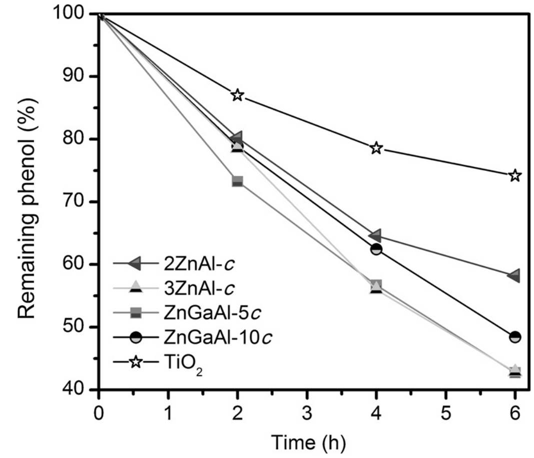

Fig. 11. Photocatalytic degradation of 80 ppm of phenol (0.85 mmol L^{-1}) by Zn(Al)O and Zn(Ga, Al)O mixed oxides, compared to Degussa P25 TiO_2.

The kinetic parameters of photocatalytic degradation reactions are frequently determined by the Langmuir–Hinshelwood model [11,47], expressed as follows:

$$r = -\frac{dC}{dt} = \frac{k_r K_{ad} C}{1 + K_{ad} C} \tag{2}$$

where k_r is the intrinsic rate constant and K_{ad} is the adsorption equilibrium constant. If the adsorption is relatively weak and the concentration is low, as in this case, the factor $K_{ad}C$ is insignificant and the equation is simplified to a pseudo-first order kinetic model, with an apparent rate constant $K_{app} = k_r K_{ad}$. The parameters K_{app} and the half-life of the compound, $t_{1/2}$, are easily calculated from the straight line obtained by plotting $\ln(C_0/C)$ *vs.* reaction time t. These parameters, as well as the linearization coefficient R^2 are reported in Table 3. All solids, except for Degussa P25 TiO_2, adjust well to this model. The smallest $t_{1/2}$ corresponds to 3ZnAl-c, closely followed by ZnGaAl-5c, 2ZnAlc and ZnGaAl-10c. Degussa P25-TiO2 presents much longer phenol half-lives. In fact, the apparent rate constant of 3ZnAl-c is exactly four times greater than the one corresponding to Degussa P25.

For the degradation of 80 ppm of phenol (Fig. 11), a similar trend in activity is observed. The solid with the greatest activity in this case is ZnGaAl-5c, very closely followed by 3ZnAl-c. The half-life of the contaminant increases in the order: ZnGaAl-5c < 3ZnAl-c < ZnGaAl-10c < 2ZnAl-c < TiO_2 (Table 3). In the best cases, close to 60% of the initial 80 ppm of phenol are degraded in 6 h.

The photoactivity of samples ZnGaAl-5c, 3ZnAl-c and ZnGaAl-10c is greater than that reported previously for MgAl LDHs impregnated with a small amount of ceria [12], which degraded nearly 50% of initial 80 ppm of phenol.

The advantages of the initial LDH phase are evidenced by the poor photocatalytic performance of two additional samples, 4ZnAl and ZnGaAl-3, tested only for comparison purposes. The as-synthesized solids presented mixed LDH and ZnO phases; the XRD patterns of the fresh and calcined solids are depicted in Fig. S4, where the ZnO impurities in the as-synthesized solids are clearly observed. After calcination, the only observable phase is ZnO, but a phase mixture of Zn(Ga, Al)O solid solution and ZnO is most likely present, in detriment of the photocatalytic performance. The sharpness of the XRD peaks of 4ZnAl-c and ZnGaAl-3c in Fig. S4 indicates that these are more crystalline solids than those derived from Zn(Ga)Al LDHs (Fig. 2).

The measured band gaps were of 3.23 eV for 4ZnAl-c and 3.20 eV for ZnGaAl-3c, both of them lower than the band gap of 3ZnAl-c (3.30 eV, Table 2). It is further interesting to observe that ZnGaAl-3c does not follow the same trend as ZnGaAl-5c and ZnGaAl-10c, where lower amounts of gallium resulted in a slightly decreased band gap (Table 2). The different behavior may be attributed to the ZnO phase.

Remarkably, these 4ZnAl-c and ZnGaAl-3c samples presented the lowest photocatalytic activity of the Zn(Ga)Al series, degrading around 50 and 62% of initial 40 ppm of phenol, respectively. At the higher concentration of 80 ppm, sample 4ZnAl-c was only slightly more active than 2ZnAl-c, degrading *ca.* 46%. Sample ZnGaAl-3c degraded only 39%. This behavior indicates that a solid solution derived from LDHs is more active than a ZnO phase.

Table 3
Langmuir–Hinshelwood kinetic parameters for the photocatalytic degradation of phenol.

Sample	40 ppm			80 ppm		
	K_{app} (h^{-1})	$t_{1/2}$ (h)	R^2	K_{app} (h^{-1})	$t_{1/2}$ (h)	R^2
2ZnAl-c	0.231	3.0	0.993	0.097	7.1	0.973
3ZnAl-c	0.264	2.6	0.999	0.141	4.9	0.996
ZnGaAl-5*c*	0.235	2.9	0.997	0.143	4.9	0.998
ZnGaAl-10*c*	0.217	3.2	0.992	0.120	5.8	0.999
TiO_2	0.066	10.5	0.581	0.054	12.8	0.956

4. Conclusions

ZnAl and ZnGaAl compounds with LDH crystalline phase were synthesized by the coprecipitation method. After calcination, mixed Zn(Ga, Al)O oxides were obtained. The only phase observable by XRD in these calcined solids is ZnO, whereas gallium and aluminum are uniformly dispersed in the oxide matrix. This dispersion provides the mixed oxide solid solutions with interesting semiconducting properties, as they present a lower band gap than pure ZnO. During the course of the photocatalytic reaction, calcined mixed oxides partially recover the original layered structure and a mixture of crystalline arrangements is observed after degradation. The photocatalytic properties of these mixed oxides are remarkably better than those of benchmark Degussa P25 TiO_2, degrading in 6 h close to 60% of initial 80 ppm of phenol, compared to *ca.* 25% degradation by P25 TiO_2. For the degradation of initial 40 ppm, sample 3ZnAl-c degraded nearly 80% in 6 h. However, neither band gap nor textural properties of the calcined solids seem to be the main parameters influencing the photocatalytic activity. Samples 3ZnAl-c and ZnGaAl-5c, with the smallest surface areas, displayed the best photocatalytic performance. Sample 3ZnAl-c, with a band gap of 3.30 eV, is more active than ZnGaAl-10c, which has a band gap of

3.18 eV. It is proposed that gallium may increase the electron–hole recombination rate. Therefore, the photocatalytic activity of LDHs could be fine-tuned by introducing different metals into the layers, as LDHs present an easy route to prepare mixed oxide solid solutions. Furthermore, the fact that LDHs degrade phenol without the addition of sacrificial reagents or pH adjustment is an important advantage of this class of materials.

Acknowledgements

This work was financially supported by the Instituto Mexicano del Petróleo. Authors thank Dr. Paz del Ángel for assistance in electron microscopy measurements. J. Prince gratefully acknowledges CONACyT for a Ph.D. scholarship. Structural models presented in the graphical abstract were drawn using the Vesta software developed by K. Momma and F. Izumi, “VESTA 3 for three-dimensional visualization of crystal, volumetric and morphology data,” J. Appl. Crystallogr., 44 (2011) 1272–1276.

Appendix A. Supplementary data

Supplementary data associated with this article can be found, in the online version, at http://dx.doi.org/10.1016/j.apcatb.2014.08.019.

References

[1] S.S. Priya, M. Premalatha, N. Anantharaman, ARPN J. Eng. Appl. Sci. 3 (6) (2008) 36–41.
[2] L.F. Liotta, M. Gruttadauria, G. Di Carlo, G. Perrini, V. Librando, J. Hazard. Mater. 162 (2009) 588–606.
[3] K. Hayat, M.A. Gondal, M.M. Khaled, S. Ahmed, A.M. Shemsi, Appl. Catal. A 393 (2011) 122–129.
[4] M. Mohamed, M.A. Barakat, Intern. J. Photoenergy 2012 (2012) 103672.
[5] A. Mantilla, F. Tzompantzi, J.L. Fernández, J.A.I. Díaz Góngora, G. Mendoza, R. Gómez, Catal. Today 148 (2009) 119–123.
[6] R. Huo, Y. Kuang, Z. Zhao, F. Zhang, S. Xu, J Colloid Interface Sci. 407 (2013) 17–21.
[7] E.M. Seftel, M. Mertens, P. Cool, Appl. Catal. B 134–135 (2013) 274–285.
[8] F. Tzompantzi, G. Mendoza-Damián, J.L. Rico, A. Mantilla, Catal. Today 220–222 (2014) 56–60.
[9] C. Li, R. Hu, L. Qin, R. Ding, X. Li, H. Wu, Mater. Lett. 113 (2013) 190–194.
[10] E.M. Seftel, M.C. Puscasu, M. Mertens, P. Cool, G. Carja, Appl. Catal. B 150–151 (2014) 157–166.
[11] J.S. Valente, F. Tzompantzi, J. Prince, J.G.H. Cortez, R. Gomez, Appl. Catal. B 90 (2009) 330–338.
[12] J.S. Valente, F. Tzompantzi, J. Prince, Appl. Catal. B 102 (2011) 276–285.
[13] E.M. Seftel, E. Popovici, M. Mertens, K. De Witte, G.V. Tendeloo, P. Cool, E.F. Vansant, Micropor. Mesopor. Mater. 113 (2008) 296–304.
[14] A. Patzko, R. Kun, V. Hornok, I. Dekany, T. Engelhardt, N. Schall, Colloid Surf. A 265 (2005) 64–72.
[15] Y. Zhao, M. Wei, J. Lu, Z.L. Wang, X. Duan, ACS Nano 3 (2009) 4009–4016.
[16] M. Shao, J. Han, M. Wei, D.G. Evans, X. Duan, Chem. Eng. J. 168 (2011) 519–524.
[17] A. Mantilla, F. Tzompantzi, J.L. Fernandez, J.A.I. Diaz Gongora, R. Gomez, Catal. Today 150 (2010) 353–357.
[18] M.E. Manríquez, E. Sánchez-Mora, J.G. Hernández-Cortez, A. Moreno-Rodriguez, T. Hernandez-Garcia, J. Phys.: Conf. Ser. 167 (2009) 012048.
[19] M.D. Hernandez-Alonso, F. Fresno, S. Suarez, J.M. Coronado, Energy Environ. Sci. 2 (2009) 1231–1257.
[20] F. Cavani, F. Trifiro, A. Vaccari, Catal. Today 11 (1991) 173–301.
[21] V. Rives, Layered Double Hydroxides: Present and Future, Nova Science Publishers, New York, 2001.
[22] J.S. Valente, R. Quintana-Solorzano, Energy Environ. Sci. 4 (2011) 4096–4107.
[23] C. Alanis Ramírez, R. Natividad Rangel, C. Barrera Díaz, J. Prince, J.S. Valente, Appl. Catal. B 140–141 (2013) 546–551.
[24] F. Figueras, Top. Catal. 29 (2004) 189–196.
[25] P.S. Kumbhar, J. Sanchez-Valente, F. Figueras, Chem. Commun. (1998) 1091–1092.
[26] F. Figueras, J. Lopez, J. Sanchez-Valente, T.T.H. Vu, J.M. Clacencs, J. Palomeque, J. Catal. 211 (2002) 144–149.
[27] K. Maeda, K. Teramura, D. Lu, T. Takata, N. Saito, Y. Inoue, K. Domen, Nature 440 (2006) 295.
[28] K. Maeda, T. Takata, M. Hara, N. Saito, Y. Inoue, H. Kobayashi, K. Domen, J. Am. Chem. Soc. 127 (2005) 8286–8287.
[29] S. Jeong, Y.-G. Ha, J. Moon, A. Facchetti, T.J. Marks, Adv. Mater. 22 (2010) 1346–1350.
[30] C.X. Xu, X.W. Sun, B.J. Chen, Appl. Phys. Lett. 84 (9) (2004) 1540–1542.
[31] J.S. Valente, E. López-Salinas, J. Prince, I. González, P. Acevedo-Peña, P. del Ángel, Mater. Chem. Phys. 147 (2014) 339–348.
[32] B.C. Meikap, G.K. Rot, J. IPHE 3 (1997) 54–61.
[33] M. Sanchez-Cantu, L.M. Perez-Diaz, A.M. Maubert, J.S. Valente, Catal. Today 150 (2010) 332–339.
[34] G.K. Schweitzer, L.L. Pesterfield, The Aqueous Chemistry of the Elements, Oxford University Press, New York, 2010.
[35] R.D. Shannon, Acta Cryst. A32 (1976) 751.
[36] B. Pourabbas, B. Jamshidi, Chem. Eng. J. 138 (2008) 55.
[37] N. Morales-Flores, U. Pal, E. Sánchez-Mora, Appl. Catal. A 394 (2011) 269–275.
[38] L. Yuliati, H. Itoh, H. Yoshida, Chem. Phys. Lett. 452 (2008) 178–182.
[39] J.J. Robbins, C. Fry, C.A. Wolden, J. Cryst. Growth 263 (2004) 283–290.
[40] J.S. Valente, E. Lima, J.A. Toledo-Antonio, M.A. Cortes-Jacome, L. Lartundo-Rojas, R. Montiel, J. Prince, J. Phys. Chem. C 114 (2010) 2089–2099.
[41] J.S. Valente, H. Pfeiffer, E. Lima, J. Prince, J. Flores, J. Catal. 279 (2011) 196–204.
[42] M.G. Álvarez, R.J. Chimentão, N. Barrabés, K. Föttinger, F. Gispert-Guirado, E. Kleymenov, D. Tichit, F. Medina, Appl. Clay Sci. 83–84 (2013) 1.
[43] F. Rouquerol, J. Rouquerol, K. Sing, Adsorption by Powders and Porous Solids, Academic Press, London, 1999.
[44] J.A. Gursky, S.D. Blough, C. Luna, C. Gomez, A.N. Luevano, E.A. Gardner, J. Am. Chem. Soc. 128 (26) (2006) 8376–8377.
[45] W.T. Reichle, S.Y. Kang, D.S. Everhardt, J. Catal. 101 (1986) 352–359.
[46] N. Ahmed, Y. Shibata, T. Taniguchi, Y. Izumi, J. Catal. 279 (2011) 123–135.
[47] M.R. Hoffmann, S.T. Martin, W. Choi, D.W. Bahnemann, Chem. Rev. 95 (1995) 69–96.